EyeHex toolbox for complete segmentation of ommatidia in fruit fly eyes

Huy Tran[1,2*], Nathalie Dostatni[2], Ariane Ramaekers[2*]

[1] Faculty of Medicine and Health Technology, Tampere University, Tampere, Finland

[2] Laboratory of Nuclear Dynamics, UMR3664, Institut Curie, Sorbonne Université, CNRS, Paris, France

* Corresponding authors

E-mails: huy.tran@tuni.fi, ariane.ramaekers@curie.fr

Abstract

Variation in *Drosophila* compound eye size is studied in various research contexts ranging from evolutionary to biomedical studies. Studying this variation requires the collection of large datasets required for the statistical power of the subsequent analyses. EyeHex is a new tool that automatically and fully segments fruit fly compound eyes from both brightfield and scanning electron microscopy images. The system comprises two modules. The first module uses machine-learning to extract the compound eye and ommatidia regions from different types of images. The second module is hard-coded and accurately determines the number and location of individual ommatidia using the hexagonal arrangement of the compound eye. EyeHex is equipped with a manual correction tool that enables control over segmentation accuracy, particularly at the edges of the eyes where ommatidia detection is more challenging due to highly slanted imaging angles and interfering ocular hairs. EyeHex is accompanied by an analysis tool to quantify ommatidia count, position, altitude, density across the eye, and arrangement along the anterior/posterior. Training and applying EyeHex model for ommatidia segmentation requires limited user inputs. It achieves a high level of accuracy (>99% when compared to manual counting) from both Scanning Electron Microscope and multi-focus brightfield images of two *Drosophila melanogaster* strains. This demonstrates that EyeHex can be integrated flexibly in a cheap and fast pipeline to extract statistics on variations of *Drosophila* compound eyes.

Keywords: Drosophila; Compound eye; Ommatidia number, Ommatidia size; Image segmentation; Morphological variation.

Background

Insect compound eyes consist of crystal-like lattices of elementary eyes, called facets or ommatidia. Each ommatidium is constituted of a fixed number of cells, including photoreceptors that sense light and transmit visual information to the brain, as well as a set of accessory cells (Nériec and Desplan, 2016; Wolff and Ready, 1993). Compound eye size varies greatly among insect groups and species due to differences in the number or diameter of individual facets. In fruit flies (*Drosophila* genus), the number of ommatidia per eye ranges from approximately 600 to 1500, while ommatidia diameter varies from approximately 15 to 22 μm (Arif et al., 2013; Gaspar et al., 2019; Keesey et al., 2019; Posnien et al., 2012; Ramaekers et al., 2019; Reis et al., 2020). Genetic variation is the primary driver of eye size variation among fruit flies, but environmental conditions such as food quality, larval density and temperature also play a role (Currea et al., 2018). On a wider phylogenetic range, the variation in eye size is much more spectacular. For example, the number of ommatidia range from 0 in some ant species for instance up to approximately 20.000 in dragonflies (Land and Nilsson, 2012).

Variation in compound eye size is investigated from various scientific perspectives, ranging from evolutionary studies to biomedical research. Evolutionary ecologists aim to identify how eye size variation affects vision and visually guided behaviors, potentially resulting in adaptation to novel ecological niches. Research has shown that larger eyes were improve vision in dim light or acuity (reviewed in (Land, 2005; Land and Nilsson, 2012; Warrant, 2008; Warrant and Nilsson, 1998). In contrast, reduced eyes are common in insects adapted to darkness, such as cave-dwelling beetles, which rely little or not at all on vision (Luo et al., 2019, 2018).

Variation in compound eye size, especially in fruit flies, is also of interest to developmental or evolutionary-developmental biologists who investigate the genetic and

developmental origins of morphological variation (reviewed in (Casares and McGregor, 2020)). Furthermore, it serves as a genetic model for human eye conditions, such as aniridia or retinitis pigmentosa (reviewed in (Gaspar et al., 2019)) and a "test-tube" for studying various human pathologies (e.g. Zika virus pathogenicity (Harsh et al., 2020) or molecular determinants of spinal muscular atrophy (Maccallini et al., 2020)).

Until now, the development of larger scale studies has been hindered by the lack of a simple, accurate, and cost-effective method to fully segment ommatidia. In most reports, ommatidia were manually counted from Scanning Electron Microscopy (SEM) images with limited throughput (Arif et al., 2013; Keesey et al., 2019; Posnien et al., 2012; Ramaekers et al., 2019). Statistical analyses that required larger datasets were performed using either estimations of ommatidia numbers (Ramaekers et al., 2019) or measurements of eye surface area or length instead of ommatidia counts (Arif et al., 2013; Harsh et al., 2020; Norry and Gomez, 2017). In a recent report, researchers applied a commercial segmentation tool (Amira v.2019.2, Thermo Fischer Scientific) to high-quality images obtained by X-ray tomography (Gaspar et al., 2020). Bright field imaging could be a desirable alternative to the more laborious and expensive SEM or X-ray tomography technologies. However, due to the prominent curvature of compound eyes, segmenting ommatidia from 2D images is non-trivial and cannot be hard coded for automatic analysis. Two features present specific challenges. Ocular bristles cover ommatidia differently in 2D eye images depending on their location on the eye surface. The level of coverage varies from minimal (e.g. in black frames, Fig. 1) to substantial (e.g. in green, blue and orange frames, Fig. 1). Additionally, dome-shaped transparent corneas act as lenses that overlay ommatidia. Consequently, ommatidia reflect light differently depending on their orientation and the angle of the incoming light, resulting in varying levels of reflection in brightfield images (Fig. 1A). A recent study on eye size variation in the *Drosophila virilis* group takes advantage of this feature, capturing and segmenting the reflection of light by each

ommatidia, rather than imaging the ommatidia themselves (Reis et al., 2020). A recent method, named Ommatidia Detection Algorithm (ODA) (Currea et al., 2023), applies Fourier Transform to detect ommatidia on images of glue eye molds, light microscopy and SEM images of various species of insects. This method pronounces the periodic patterns of ommatidia in the compound eyes with filters in the frequency domain of the images. However, these methods have limitations at the edge of the eye, where ommatidia are imaged at very slanted angles. At these angles, there might be no reflections of light sources, or the reflections are heavily displaced from the center of the ommatidia. Additionally, ocular hairs near the edges become visible from top-down imaging and interfere with the ommatidia local patterns (Fig. 1).

In this report, we present a complete EyeHex toolbox for the automatic segmentation of ommatidia in fruit fly compound eyes. EyeHex comprises two modules (Fig. 2): The first module uses a machine learning-based classification tool (Trainable Weka Segmentation, ImageJ (Arganda-Carreras et al., 2017) to delimit the compound eye from the background. Users can define the training data for the classification, making it applicable to a wide range of image types, from brightfield and SEM images in various settings. The second module is hard-coded and takes advantage of the hexagonal organization of the compound eye to accurately determine the location and the number of ommatidia., EyeHex achieves a high level of

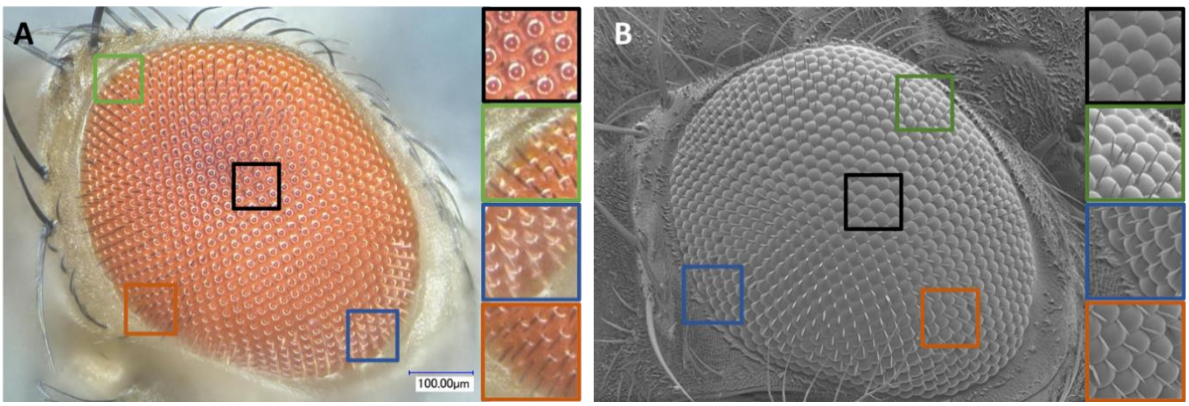

Figure 1. The many facets of the eye**.** Due to the convex structure of the compound eye, the aspect of ommatidia observed on 2D images varies greatly in different eye regions. Images shown here were acquired using (A) a macroscope (this study) and (B) by SEM (Ramaekers et al., 2019). The zoom-in regions are shown on the right side of each panel with the corresponding frame colors. Note the differences in reflection, shape and inter-ommatidial hair aspect.

accuracy, with over 99% accuracy when compared to manual counting, including from images obtained with brightfield microscopy. It requires limited user input, making it a cost-effective and efficient method for characterizing variations in *Drosophila* eye size.

Methods

Workflow

The EyeHex toolbox protocol consists of two successive steps: (1) Training and Classification, and (2) Segmentation (Fig. 2):

Training and Classification: A first set of 2D sample image(s) is used as training data for the classification of the eye area and facet surfaces (vs. facet boundaries) (module A, Fig. 2). This is performed taking advantage of an assisted-segmentation tool to manually delimit the compound eye area and segment small groups of ommatidia located at different positions

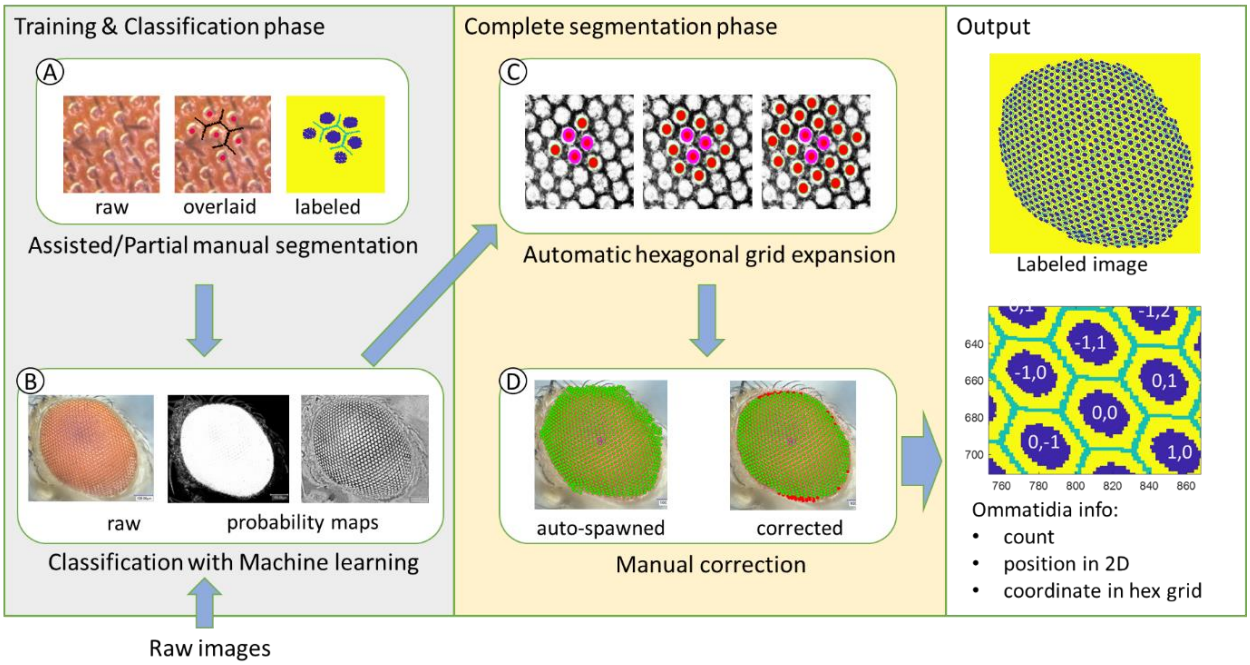

Figure 2. Overview of ommatidia segmentation steps using EyeHex toolbox. The process consists of two phases. The '*Training and Classification phase'* involves the generation of the training data with the assisted segmentation of a subset of ommatidia (module A) for the machine learning module, which converts raw input images into probability maps of the eye region and facet region (module B). In the *'Complete segmentation phase'*, ommatidia are automatically and exhaustively segmented by expanding a hexagonal grid to fit the facet probability map within the eye region (module C). The user then validates and manually corrects this ommatidia grid using a provided graphical user interface (module D). The outputs include the labelled images for the ommatidia facet and boundary regions (top right), the ommatidia count and the location of each individual ommatidium (bottom right).

(e.g., center vs edges), thus presenting different shapes and reflections (Fig. 1A). The machine learning module will next use this training data to convert each raw input image into probability maps of eye area and facets surfaces (module B, Fig. 2).

Segmentation: Next, ommatidia will be automatically and comprehensively segmented by expanding a hexagonal grid to fit a facet probability map within the eye area classified as described above (module C, Fig. 2). Users can validate and manually correct the segmentation process for each image using the provided Graphical User Interface (GUI, module D, Fig. 2). The output of the segmentation consists of (1) a labeled image carrying the information on the location of ommatidia surfaces and boundaries, (2) the count of ommatidia number and (3) data on each ommatidium (2D position and coordinates on the hexagonal grid), for further analysis.

Data acquisition

Drosophila strains and culture:

Fly stocks were cultured on standard cornmeal diet food at 25°C in density -controlled conditions: batches of 10 females and males were raised at 25°C and transferred into a fresh vial every day. For each vial, eye measures were performed only on females eclosing during the first two days of eclosion. Genotypes used in this study were: Canton-S^{BH} (Ramaekers et al., 2019); Hikone-AS (Kyoto DGRC 103421).

Scanning electron microscopy (SEM) images:

SEM images are reused from (Ramaekers et al., 2019).

Light-microscopy images (this study):

Light microscopy images were acquired from non-fixed, freshly cut adult heads glued laterally on glass slides using a solvent-free all material glue (UHU® - cat #64481). 3D images stacks (Z distance = 8 μm) were acquired at 400-600X magnification with a Keyence digital

microscope VHX 2000 using optical zoom lens VH-Z20R/W. Single focused 2D images were generated using Stack Focuser plugin from ImageJ (Schindelin et al., 2012).

Automatic compound eye and ommatidia classification with machine learning

Training data preparation:

This step is performed only when a new type of image (e.g., SEM, brightfield microscope…) is introduced. Users' attention is required to identify ommatidia on different regions of the compound eye from focused 2D image samples, assisted by the GUI included in the EyeHex toolbox (module A, Fig. 2). We found that accurate classification can be achieved with a training set as small as two images.

Automatic classification:

Classification is performed using the Fiji Weka plug-in (Arganda-Carreras et al., 2017). Training datasets are used to train two separate pixel-based Fast Random Forest classifiers, each containing 100 decision trees (Breiman, 2001). The trained classifier will then convert the focused 2D images into probability maps of the eye area and the ommatidia surfaces. The compound eye region is defined by thresholding the eye probability map with the Otsu algorithm (Otsu, 1979).

Automatic segmentation

The ommatidia hexagonal grid

Segmentation is performed by taking advantage of the remarkably robust hexagonal organization of the compound eye, allowing to map each ommatidium to a unique coordinate on a hexagonal grid. Thus, each ommatidium is characterized by two sets of coordinates: an integer coordinate (x_{hex}, y_{hex}) on the hexagonal grid and a continuous Cartesian coordinate (x, y) on the 2D ommatidia probability map (Fig. 3A). Note that each ommatidium of the

hexagonal grid shares edges with 6 neighbors, instead of 4 as in a normal orthogonal grid. The segmentation process includes three steps:

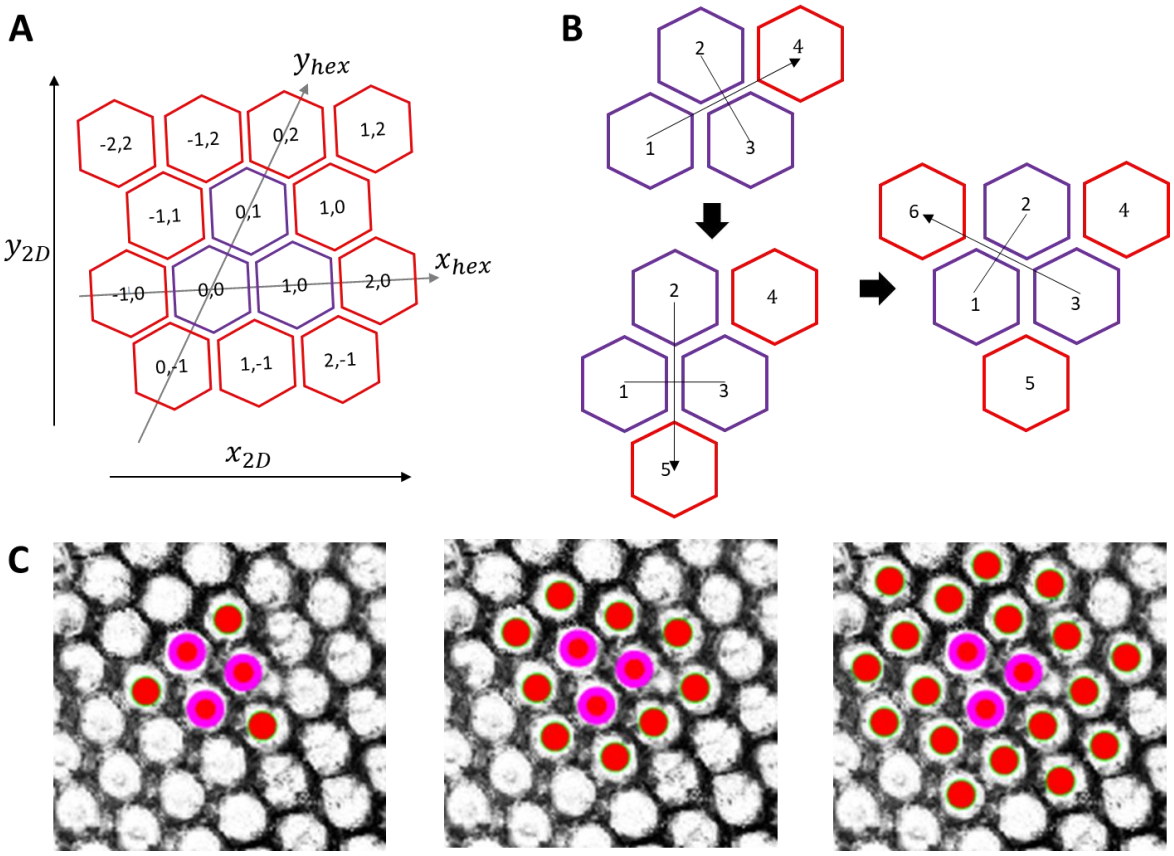

Figure 3. The ommatidia hexagonal grid. (A) The grid is seeded from three original ommatidia (purple). Each ommatidium is identified by a unique integer coordinate (x_{hex}, y_{hex}) on the hexagonal grid, alongside its continuous Cartesian coordinate (x, y) on the ommatidia probability map. It is important to note that the x_{hex} axis and the x axis are not necessarily parallel. (B) New ommatidia (red) are added individually to the grid by mirroring the seed ommatidia (purple): ommatidium 4 is spawned by mirroring ommatidium 1 through ommatidium 2 and 3; ommatidium 5 by mirroring ommatidium 2 through ommatidium 1 and 3 and ommatidium 6 by mirroring ommatidium 3 through ommatidium1 and 2. (C) New ommatidia (red solid circles) are segmented and added to the outer row of existing hexagonal grid set by 3 seed ommatidia (purple), shown here on top of the ommatidia probability map I_{prob} generated during classification phase.

Step 1: Setting the origin and orientation of the hexagonal grid:

The origin and orientation of the grid are established based on three original ommatidia adjacent to one another (purple cells in Fig. 3A; with coordinates (x_{hex}, y_{hex}) equal to (0,0), (1,0), (0,1)), selected by the user at the center of compound eye.

Step 2: Expansion of the hexagonal grid:

The hexagonal grid is expanded by adding individual ommatidia to the current grid. For each three adjacent ommatidia (referred as omtd1, omtd2, omtd3 ; purple cells in Fig. 3B), we have their respective coordinates on the hexagonal grid (x_{hex1}, y_{hex1}), (x_{hex2}, y_{hex2}), (x_{hex3}, y_{hex3}) and on the Cartesian grid (x_1, y_1), (x_2, y_2), (x_3, y_3). Those coordinates are used to predict the position of a fourth ommatidium, omtd4, which mirrors omtd1 through omtd2 and omtd3 (Fig. 3B) via Eq. 1-4:

$$x_{hex4} = x_{hex2} + x_{hex3} - x_{hex1}, \tag{1}$$

$$y_{hex4} = y_{hex2} + y_{hex3} - y_{hex1}, \tag{2}$$

$$x_4 = x_2 + x_3 - x_1, \tag{3}$$

$$y_4 = y_2 + y_3 - y_1. \tag{4}$$

Based on the ommatidia probability map, the program will find an ommatidium within the vicinity of the mirrored position (x_4, y_4) and add omtd4 to the hexagonal grid at the coordinates (x_{hex4}, y_{hex4}) (see below). Only the closest ommatidium within a distance of $L_{grid}/2$ from the predicted position (x_4, y_4) is added to the grid. Here, L_{grid} is the average length of the hexagonal ommatidial edges:

$$L_{grid} = \sum_{i,j=1..3} \frac{(x_i - x_j)^2 + (y_i - y_j)^2}{6}. \tag{5}$$

During the automatic hexagonal expansion (Fig. 3C), new ommatidia close to the mirrored position that best fits the ommatidia facet probability map (see below) will always be added to the perimeter of the grid, unless they are found outside the compound eye region (Fig. 3C).

<u>Fitting new ommatidia to the ommatidia probability map</u>

From the three adjacent ommatidia (omtd1, omtd2, omtd3), we look for the position of omtd4 (x_4, y_4) based on the facet probability map (denoted as $I_{prob}(x, y)$) generated with the

machine learning module. The general strategy is "find Mickey pattern" with omtd2 and omtd3 being the "ear" and omtd4 being the "face". A template image I_{mouse} of size $m \times m$ (m in pixel) is constructed with three filled identical circles of radius 0.225$\times m$, the centers of which form a perfect angle with edge $0.5 \times m$ (Fig. 4A). The pattern is then smoothened with a 2D gaussian filter with σ=$m/20$. We also set an "ignore" region (with *NaN* pixel value, dashed blue in Fig. 4A) on I_{mouse} to avoid interference from surrounding ommatidia.

We called (x'_2, y'_2), (x'_3, y'_3) and (x'_4, y'_4) the coordinates of the centers of the three circles in the template image I_{mouse}. We find a linear transformation $[M]_B^{B'}$ from the coordinate vectors B' to the coordinate vectors B, in which:

$$B' = [v'_a \quad v'_b] = \begin{bmatrix} x'_4 - x'_2 & x'_4 - x'_3 \\ y'_4 - y'_2 & y'_4 - y'_3 \end{bmatrix} \tag{6}$$

and $B = [v_a \quad v_b] = \begin{bmatrix} x_4 - x_2 & x_4 - x_3 \\ y_4 - y_2 & y_4 - y_3 \end{bmatrix}$. (7)

For each non-*NaN* pixel in position (i, j) in I_{mouse}, we find the corresponding coordinate $[M]_B^{B'}(i, j)$ on I_{prob} (Fig. 4B).

The objective function for the fit of the new omtd4 position $\Delta(x_4, y_4)$ is given by the squared error between the facet probability map and the transformed mouse image:

$$\Delta(x_4, y_4) = \sum_{i,j=1..m} \left(I_{prob}([M]_B^{B'}(i, j)) - \theta \times I_{mouse}(i, j) \right)^2 , \tag{8}$$

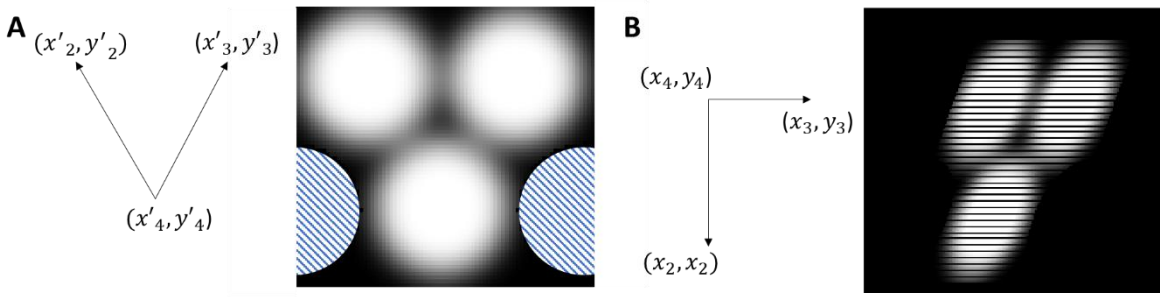

Figure 4. '*Mickey patterns*' on the facet probability map. (A) The coordinate vectors $B' = (v'_a, v'_b)$ (left) for the mouse image I_{mouse} (right). The objective function does not take into account the blue dashed regions (NaN value). (B) Example of the new coordinate vectors $B = (v_a, v_b)$ from ommatidium 2, ommatidium 3 and ommatidium 4 position (left) with the transformed I_{mouse} in this coordinate (right).

with θ being a free parameter to adjust for pixel brightness.

Due to frequent irregularities on the probability map, we introduce additional constraints to preserve the integrity of the hexagonal grid and account for the fact that the facet orientation changes gradually along the grid: The objective function $\Delta(x_4, y_4)$ is set to infinity when the new omtd4 position is farther than $0.3 \times L_{grid}$ from the predicted position that mirrors omtd1, and when the omtd4 top view angle is too steep (<20°) or too different from that of omtd1.

Manual correction

Following the automatic hexagonal grid expansion, users can use the provided GUI to manually remove or add new ommatidia if needed. After manual correction, newly added ommatidia will be mapped and get their own coordinate in the existing hexagonal grid.

Segmentation outputs

Following the complete segmentation process, EyeHex exports per eye image its segmented ommatidia (binary) mask. Also exported is the csv file containing information about each ommatidium's index, its Cartesian and hexagonal coordinates.

Data analyses

Once the segmentation with EyeHex for every image in the dataset is completed, a MATLAB analysis script (see Supplementary Material) can be run to automatically extract compound eye's features further and provide the population's statistics.

Measures of ommatidia size

When using multi-focused brightfield images, the z-coordinate of each ommatidium can be determined based on its position in the original stack of images. We use this information to estimate the size of an ommatidium by averaging its Euclidean distances in the three-dimensional space to its adjacent ommatidia. These values are then used to generate a contour map of local variations in ommatidia size across the eye, as shown in Fig. 5C.

Column detection and profiles

The ommatidia are arranged in columns that reflect the progressive specification of R8 ommatidia founder cells along the anterior-posterior axis of the eye primordium (eye-antennal disc). To locate these columns, the segmented grid is reoriented so that the x-axis on the hexagonal grid runs from the dorsal posterior to the ventral anterior part of the eye (as shown in Fig. 5D). The new x_{hex} coordinate of the ommatidia defines a column number, that corresponds to its birth order during R8 specification. From the new reoriented grid, we calculate the "column profile" as the ommatidia number per column, which informs on the eye geometry.

Results

The EyeHex toolbox

The EyeHex toolbox is a set of MATLAB scripts that allows users to automatically segment of all visible ommatidia from 2D images of *Drosophila* compound eyes. Segmentation occurs in two successive steps, as summarized in Fig. 2. The first step, '*Training and*

Classification' uses machine learning to translate raw 2D images into probability maps of the eye region and ommatidia localization. It requires prior manual segmentation of classification training data (Fig. 2A). During the "*Segmentation*" step, ommatidia are automatically and exhaustively segmented by expanding a hexagonal grid to fit the ommatidia probability map within the eye region (module C). This last step can be manually refined (Fig. 2D). Minimal user intervention is required in each of the two phases via a Graphical User Interface (GUI). EyeHex output includes labeled eye images depicting the ommatidia masks (Fig. 2E), as well as ommatidia counts and positions in csv format (Fig. 2F). The toolbox, its manual and sample images are available for download on GitHub at https://github.com/huytran216/EyeHex-toolbox.

Segmentation on SEM and brightfield image

The compound eyes of female *Drosophila melanogaster* flies raised in standard laboratory conditions typically consist of 700 to 800 ommatidia. The EyeHex toolbox was applied to already published scanning electron microscopy (SEM) (Ramaekers et al., 2019) images and newly acquired brightfield macroscope images (Table 1) on two *Drosophila melanogaster* highly inbred laboratory stocks (Hikone-AS and Canton-S^{BH}). For the sake of comparison, we also reproduce published data from the same study on fully manual or estimated counts of ommatidia numbers, for the same two strains. Independent training datasets were generated for both SEM and brightfield images to enable machine learning-based classification. To achieve this goal, we manually segmented approximately 80 ommatidia, which represents around 10% of the total number of ommatidia per eye, in a single image (SEM or brightfield). We then proceeded with the classification, automatic segmentation and counting (Table 1).

Table 1. Ommatidia counts on SEM and brightfield images.

	SEM (Hikone-AS)	Brightfield (Hikone-AS)	Brightfield (Hikone-AS)	Brightfield (Canton-S^{BH})	Brightfield (Canton-S^{BH})
Data collection	*Ramaekers et al. 2019*	*Ramaekers et al. 2019*	*This study*	*Ramaekers et al. 2019*	*This study*
n	*6*	*16*	*26*	*15*	*12*
Ommatidia Nb *EyeHex automatic count, no correction*	722 ± 26.2	/	774.3 ± 24.7	/	807.2 ± 24.4
Ommatidia Nb *EyeHex automatic count, with correction*	740 ± 21.8	/	749.7 ± 17.5	/	830.6 ± 20.5
Ommatidia Nb *Ramaekers et al., 2019*	742 ± 20.2 *Manual count*	736.0 ± 27.09 *Estimation*	/	828.0 ± 34.0 *Estimation*	/

Ommatidia counts (Mean ± Standard Deviation) for sets of SEM or brightfield images. Images were either reused from a previous study (Ramaekers et al., 2019) or newly collected. We compare ommatidia counts performed using EyeHex segmentation with or without manual correction together with previous counts or estimations (Ramaekers et al.,2019). They were generated using automatic EyeHex segmentation without or with manual correction. As a comparison, we provide the manual counts on SEM images published in Ramaekers et al., 2019.

We first compared the ommatidia counts obtained with EyeHex from SEM images, with the previously reported manual counts performed on the same dataset. The mean and standard deviation of the ommatidia counts from EyeHex automated segmentation were up to 97% accurate when compared to the manual counts. Accuracy increased up to 99.7% with minimal manual correction (Fig. 2D). For brightfield images, our previous study only reported estimations (see Ramaekers et al., 2019 for the method) but no direct manual counts. Here, we counted ommatidia with EyeHex, with or without manual correction, on newly acquired brightfield images of both Hikone-AS and Canton-S^{BH} images. Those images are less contrasted in comparison to SEM images, requiring manual correction to improve the segmentation at the edges of the eye. However, those corrections were limited as they corresponded to approximately 7% of ommatidia either added, removed, or adjusted at the edges of the compound eye. It is worth noting that the two laboratory stocks Hikone-AS and Canton-S^{BH} may have varied between the previous and current study, which were carried out more than 5 years apart, possibly because of genetic drift. Therefore, we did not expect the

ommatidia counts from these two datasets to be identical. Nevertheless, EyeHex measurements were very close to our previous data. Interestingly, the statistics of EyeHex measurements on brightfield images are close to the ones of manual counts on SEM images, which are the most reliable measurements of ommatidia numbers. This indicates that the use of brightfield images combined with the EyeHex method provides an accurate representation of biological samples. This is in contrast with our previous counts on brightfield images that were using the surface area of an ellipse as an estimation (Table 1).

Ommatidia size profile and ommatidia column count

Characterizing the exact position of individual ommatidia within the eye provides quantitative measurements of distinct morphological features that can be quantified to assess the effects of genetic and environmental changes on eye development, and strongly influence vision. Because brightfield images are acquired as stacks of multiple focal planes, the position of each ommatidium in the Z-axis (altitude) can be determined in addition to its coordinates in the 2D image (X and Y axes, see example in Fig. 5A-B). We can also estimate the local ommatidial density across the eye by calculating the average distance in 3D space between each ommatidium and its 6 adjacent neighbors. This feature is proportional to the diameter of individual ommatidia and the inter-ommatidial angles across the whole eye, two features that strongly influence important visual properties, such as contrast sensitivity and acuity (Land, 1997) (Land and Nilsson, 2012). For all eyes analyzed, as the example in in Figure 5, ommatidia density varies within a 20% range, along the posterior-dorsal (upper left) and anterior-ventral (lower right) axis of the eye, in agreement with local observations in (Gaspar et al., 2020). However, along the posterior-ventral (lower left) and anterior-dorsal (upper right) axis of the eye, the difference in ommatidia density can be up to 2-fold.

Characterizing the variability of ommatidia number and location may provide crucial insights into the robustness of eye developmental processes. For example, ommatidia are arranged in regularly spaced columns along the anterior-posterior (A-P) axis of the eye (Fig. 5D). This organization reflects the progressive determination and spacing of ommatidia founder cells (termed R8 cells) along the A-P axis of the eye primordium during the progression of a differentiation wave named '*morphogenetic furrow*' (Ready et al., 1976) (Wolff and Ready, 1993) (for a recent review, see (Warren and Kumar, 2023)). Thus, quantifying the number of A-P columns in the adult eye may provide a read-out of the R8 determination process. We used EyeHex to extract this information from a set of brightfield eye images from

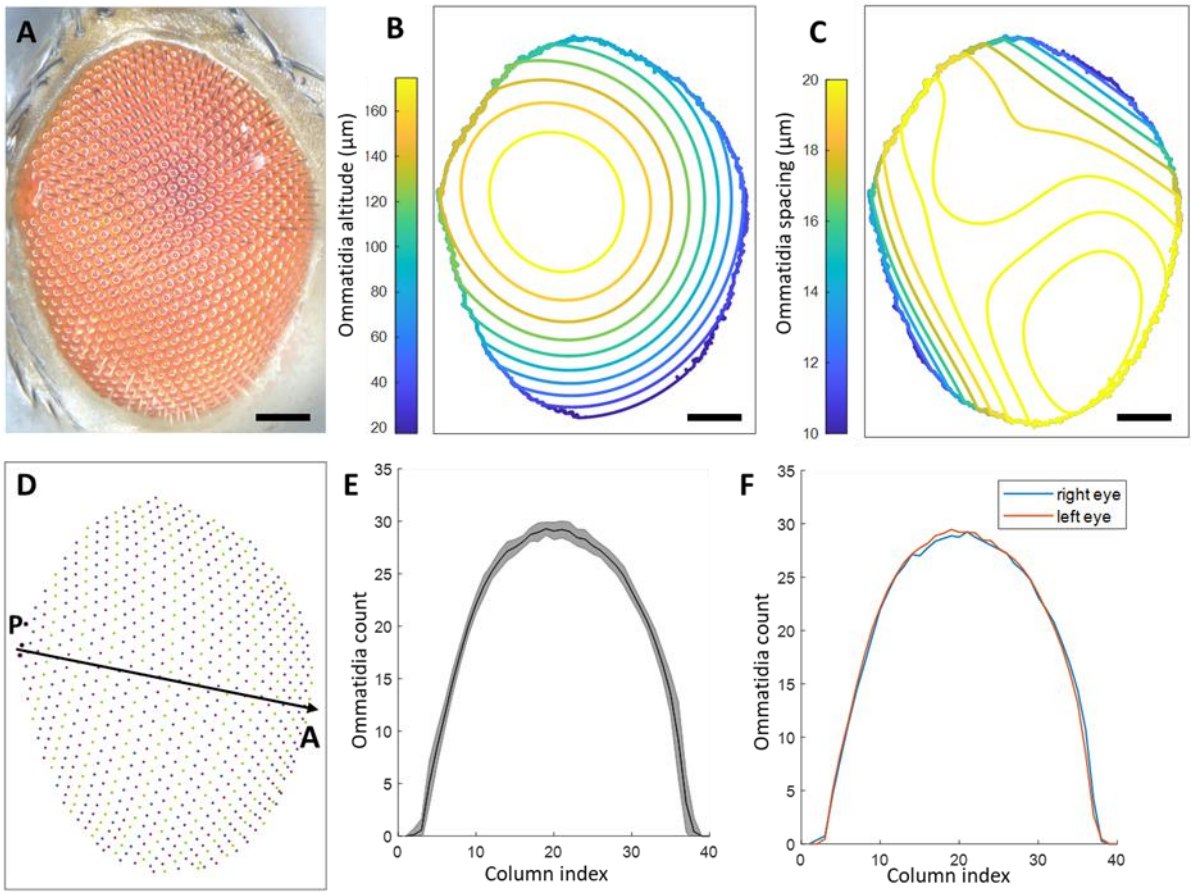

Figure 5. EyeHex output: Quantitative analysis of compound eye features. A) Brightfield eye image analyzed in panels B and C. B) Contour map of ommatidia altitude (in µm, calculated relative to the lowest focal plane). C) Contour map of estimated spacing between individual ommatidia (in µm). D) Anterior (A) to posterior (P) columns of detected ommatidia, separated by colors, with those in the most posterior column highlighted in bold. E) Ommatidia count in each column from posterior (P) to anterior (A) (line and shade represent respectively the mean and standard deviation); sample size is *n*=26. F) Comparison of mean ommatidia count profiles between left (blue curve, n =19) eyes and right (red curve, n=7) eyes. Scale bars in A to C: 100 µm.

26 individuals of the Hikone-AS wild-type genetic background. Each eye consisted of 33.89 ± 1.05 columns (mean and standard deviation). We also extracted '*column profiles*' by plotting the number of ommatidia per column along the A-P axis of the eye (Fig. 5D). We then aligned the 26 column profiles for comparison. The mean aligned column profile from 26 brightfield eye images is shown in Figure 5E. Interestingly, the standard deviation (shaded area of the plot, Fig. 5E) of the mean is on average ~1.08 ommatidia, with a maximum of 3.73 ommatidia per column. Therefore, the highly inbred Hikone-AS laboratory individuals show very little variation in eye organization and size, indicating that despite its complexity, compound eye development is remarkably robust. Comparison of the mean aligned column profiles between left and right eyes from separate individuals also did not reveal any significant bias (an average difference of 0.45 ommatidia per column) (Fig. 5F).

Discussion

The EyeHex toolbox automatically segments ommatidia from fruit fly compound eyes and locates individual ommatidia in 2D space. In combination with a dedicated analysis pipeline, it provides multiple quantitative features characterizing the eye organization, including total ommatidia counts, ommatidia count profiles across the A-P axis, and contour maps of individual ommatidia size and altitude. EyeHex is applicable to multiple image types, including brightfield and SEM images. The system consists of two modules, one that employs machine learning to identify the position of the eye and ommatidia, and another that automatically segments the ommatidia by placing them on a hexagonal grid. A manual correction interface is available to ensure the quality of the segmentation, and to make any necessary corrections.

Manual ommatidia counts on compound eye images acquired by SEM are considered the gold standard for ommatidia counts. Automated segmentation with EyeHex on a set of SEM images

produced ommatidia counts that matched the manual measures with an accuracy of 99.7 % after minor manual corrections. When applied to brightfield images, acquired with a macroscope on non-fixed samples, EyeHex generated data with statistics very similar to those obtained on SEM images, whether counted by EyeHex or manually. Thus, high accuracy levels were maintained, with simpler and faster sample preparation and image acquisition, and automated image processing. Published data on fruit fly ommatidia size were determined by averaging the diameter or surface area of one or several small groups of ommatidia located at specific positions of the eye (Gaspar et al., 2020; Keesey et al., 2019; Posnien et al., 2012; Ramaekers et al., 2019). In contrast, our analysis tool measures ommatidia size by calculating the distance between adjacent ommatidia in 3D space, taking into account the altitude of individual ommatidia in addition to their position in 2D. This provides accurate measures of ommatidia size throughout the entire eye, even at edges, where imaging angles are most slanted.

Various tools have been developed to automatically segment ommatidia from different types of images. In Gaspar *et al*. (Gaspar et al., 2020), ommatidia are treated as independent cells with a predefined minimum spacing between them. However, this approach does not take into account their hexagonal organization, which can lead to false negatives where damaged or non-reflective ommatidia are not registered. Currea *et al.* (Currea et al., 2023) proposed a method that exploits the repeating ommatidia patterns of compound eyes by filtering on the frequency domain. This semi-global approach sequentially fits hexagonal or orthogonal grids to overlapping regions of the eyes and recombines them into a single grid. However, this method may produce errors when dealing with extreme eye warping, which is common at the edges of the compound eye. The EyeHex toolbox performs ommatidia segmentation on an *ad-hoc* basis, where new ommatidia are identified one-by-one and added to the existing grid based on the three nearest registered ommatidia. This method can overcome local warps in the compound

eye surface while preserving the hexagonal ommatidia organization at the larger scale. Nevertheless, no automatic segmentation method can achieve 100% accuracy. The number of ommatidia in inbred flies are highly reproducible, with a relative standard deviation of less than 2% (this study, (Currea et al., 2018; Gaspar et al., 2020). Therefore, achieving near-perfect ommatidia segmentation is essential for any study on the morphological variation of the compound eye. As a result, the inspection and manual correction by users, as implemented in the EyeHex toolbox, remain indispensable.

EyeHex's hexagonal grid can morph freely and account for non-uniform ommatidia spacing, enabling precise measurements of ommatidia size at the edges of the eye where they are imaged at slanted angles. This feature also allows accommodating subtle disruptions or irregularities of the eye lattice, as might occur in some mutants. However, since ommatidia are mapped to the hexagonal coordinates, mutant eyes with gross structural abnormalities might not be accurately segmented by EyeHex. In this study, EyeHex was tested solely on *Drosophila melanogaster* samples but we do not anticipate any significant challenges when applying it to other *Drosophila* species. Limitations may arise with highly bulged eyes, where the edges are not visible in brightfield image stacks. Imaging of such bulgy eyes requires the use of different imaging techniques such as μCT scans (Gaspar et al., 2020) or indirect imaging of molds of eyes flattened by incision (Ramirez-Esquivel et al., 2017). For these types of data, a separate tool will be needed to reconstruct the 2d flatten image of the intact eye, which is not currently implemented in EyeHex toolbox.

Acquiring larger sets of accurate quantitative data on compound eye features will facilitate large scale characterization of eye size variation within and between species. It will also open the way to studies addressing developmental instability and robustness. In fruit flies, such studies have mainly focused on traits such as wing morphology and mechanosensory hair patterns, as they are easier to quantify (see for instance (Debat et al., 2009; Polak and Starmer,

2001). However, the compound eye with its well described development would constitute an ideal system to investigate these questions. Although compound eyes are the most common type of eyes, they present poor acuity in comparison to camera eyes, such as the vertebrate eye (Kirschfeld, 1976; Land, 1997; Mallock, 1894). To achieve a similar resolution to human eyes, compound eyes would need to be composed of millions of ommatidia, reaching a radius of 6 meters. To compensate for this poor acuity, many compound eyes present localized 'acute zones' with larger ommatidia. This increases acuity for specific parts of the visual field, adapted to the species' ecology (Land, 1997). Although this trait is ecologically and evolutionarily relevant, previous reports of eye size variation in the *Drosophila* genus have only provided data on a single (or more recently three) group of ommatidia (Gaspar et al., 2020; Keesey et al., 2019; Posnien et al., 2012; Ramaekers et al., 2019). By localizing individual ommatidia on a 3D space, EyeHex generates a contours map of ommatidia size across the entire eye, which can be used to identify potential acute zones or more subtle local patterns of variation of ommatidia size.

Variation in fruit fly compound eye size is an important model in the field of evolutionary developmental biology (Casares and McGregor, 2020). Numerous cases of eye size variation were documented in fruit flies and the development of *Drosophila* compound eye development is particularly well described. Moreover, it also used as a test tissue in biomedical studies. Our toolbox EyeHex provides a complete solution for accurate segmentation of fruit fly eyes, from a variety of image types, including from brightfield images, that can be used to extract a variety of statistics regarding compound eye morphology. It thus provides a flexible, accurate and cost-effective pipeline to characterize compound eye morphological variation, which should further facilitate the use of this system as a model.

List of abbreviations

A-P: Anterior-Posterior

μCT: Micro Computed Tomography

SEM: Scanning Electron Microscopy

GUI: Graphical User Interface

Declarations

Ethics approval and consent to participate

Not applicable

Consent for publication

Not applicable

Availability of data and Supplementary materials

EyeHex toolbox is available from https://github.com/huytran216/EyeHex-toolbox.

The analysis code following EyeHex segmentation for all eyes in the dataset can be downloaded from https://github.com/huytran216/EyeHex_analysis.

Segmentation results and analysis for Hikone-AS (26 eyes) and Canton-S^{BH} (12 eyes): Supplementary_file.pdf

Competing interests

The authors declare that they have no competing interests.

Author's contributions

AR collected the data (sample preparation and imaging), HT created EyeHex toolbox and analyzed the data, AR and HT interpreted the data. AR, HT and ND drafted the manuscript.

Acknowledgments

The authors want to thank Virginie Courtier (CNRS, Institut Jacques Monod, Paris) for providing access to the Keyence macroscope.

References

Arganda-Carreras, I., Kaynig, V., Rueden, C., Eliceiri, K.W., Schindelin, J., Cardona, A., Sebastian Seung, H., 2017. Trainable Weka Segmentation: a machine learning tool for microscopy pixel classification. Bioinformatics 33, 2424–2426. https://doi.org/10.1093/bioinformatics/btx180

Arif, S., Hilbrant, M., Hopfen, C., Almudi, I., Nunes, M.D.S., Posnien, N., Kuncheria, L., Tanaka, K., Mitteroecker, P., Schlötterer, C., Mcgregor, A.P., 2013. Genetic and developmental analysis of differences in eye and face morphology between Drosophila simulans and Drosophila mauritiana. Evolution and Development 15, 257–267. https://doi.org/10.1111/ede.12027

Breiman, L., 2001. Random Forests. Machine Learning 45, 5–32. https://doi.org/10.1023/A:1010933404324

Casares, F., McGregor, A.P., 2020. The evolution and development of eye size in flies. Wiley Interdisciplinary Reviews: Developmental Biology. https://doi.org/10.1002/wdev.380

Currea, J.P., Smith, J.L., Theobald, J.C., 2018. Small fruit flies sacrifice temporal acuity to maintain contrast sensitivity. Vision Research 149, 1–8. https://doi.org/10.1016/j.visres.2018.05.007

Currea, J.P., Sondhi, Y., Kawahara, A.Y., Theobald, J., 2023. Measuring compound eye optics with microscope and microCT images. Commun Biol 6, 1–12. https://doi.org/10.1038/s42003-023-04575-x

Debat, V., Debelle, A., Dworkin, I., 2009. PLASTICITY, CANALIZATION, AND DEVELOPMENTAL STABILITY OF THE DROSOPHILA WING: JOINT EFFECTS OF MUTATIONS AND DEVELOPMENTAL TEMPERATURE. Evolution 63, 2864–2876. https://doi.org/10.1111/j.1558-5646.2009.00774.x

Gaspar, P., Almudi, I., Nunes, M.D.S., McGregor, A.P., 2019. Human eye conditions: insights from the fly eye. Human Genetics 138, 973–991. https://doi.org/10.1007/s00439-018-1948-2

Gaspar, P., Arif, S., Sumner-Rooney, L., Kittelmann, M., Bodey, A.J., Stern, D.L., Nunes, M.D.S., McGregor, A.P., 2020. Characterization of the genetic architecture underlying eye size variation within drosophila melanogaster and drosophila simulans. G3: Genes, Genomes, Genetics 10, 1005–1018. https://doi.org/10.1534/g3.119.400877

Harsh, S., Fu, Y., Kenney, E., Han, Z., Eleftherianos, I., 2020. Zika virus non-structural protein NS4A restricts eye growth in *Drosophila* through regulation of JAK/STAT signaling. Disease Models & Mechanisms dmm.040816. https://doi.org/10.1242/dmm.040816

Keesey, I.W., Grabe, V., Gruber, L., Koerte, S., Obiero, G.F., Bolton, G., Khallaf, M.A., Kunert, G., Lavista-Llanos, S., Valenzano, D.R., Rybak, J., Barrett, B.A., Knaden, M., Hansson, B.S., 2019. Inverse resource allocation between vision and olfaction across the genus Drosophila. Nature Communications 10, 1–16. https://doi.org/10.1038/s41467-019-09087-z

Kirschfeld, K., 1976. The Resolution of Lens and Compound Eyes, in: Zettler, F., Weiler, R. (Eds.), Neural Principles in Vision, Proceedings in Life Sciences. Springer, Berlin, Heidelberg, pp. 354–370. https://doi.org/10.1007/978-3-642-66432-8_19

Land, M.F., 2005. The optical structures of animal eyes. Current Biology 15, R319–R323. https://doi.org/10.1016/j.cub.2005.04.041

Land, M.F., 1997. VISUAL ACUITY IN INSECTS. Annu. Rev. Entomol. 42, 147–177. https://doi.org/10.1146/annurev.ento.42.1.147

Land, M.F., Nilsson, D.-E., 2012. Animal Eyes, Oxford Animal Biology Series. Oxford University Press, Oxford.

Luo, X.Z., Antunes-Carvalho, C., Wipfler, B., Ribera, I., Beutel, R.G., 2019. The cephalic morphology of the troglobiontic cholevine species Troglocharinus ferreri (Coleoptera, Leiodidae). Journal of Morphology 280, 1207–1221. https://doi.org/10.1002/jmor.21025

Luo, X.-Z., Wipfler, B., Ribera, I., Liang, H.-B., Tian, M.-Y., Ge, S.-Q., Beutel, R.G., 2018. The cephalic morphology of free-living and cave-dwelling species of trechine ground beetles from China (Coleoptera, Carabidae). Org Divers Evol 18, 125–142. https://doi.org/10.1007/s13127-017-0351-5

Maccallini, P., Bavasso, F., Scatolini, L., Bucciarelli, E., Noviello, G., Lisi, V., Palumbo, V., D'Angeli, S., Cacchione, S., Cenci, G., Ciapponi, L., Wakefield, J.G., Gatti, M., Raffa, G.D., 2020. Intimate functional interactions between TGS1 and the Smn complex revealed by an analysis of the Drosophila eye development. PLoS Genet 16, e1008815. https://doi.org/10.1371/journal.pgen.1008815

Mallock, A., 1894. I. Insect sight and the defining power of composite eyes. Proceedings of the Royal Society of London 55, 85–90. https://doi.org/10.1098/rspl.1894.0016

Nériec, N., Desplan, C., 2016. From The Eye To The Brain: Development Of The Drosophila Visual System. Curr Top Dev Biol 116, 247–271. https://doi.org/10.1016/bs.ctdb.2015.11.032

Norry, F.M., Gomez, F.H., 2017. Quantitative trait loci and antagonistic associations for two developmentally related traits in the drosophila head. Journal of Insect Science 17, 19. https://doi.org/10.1093/jisesa/iew115

Otsu, N., 1979. A threshold selection method from gray-level histograms. IEEE Transaction on System, Man and Cybernetics C, 62–66. https://doi.org/10.1109/TSMC.1979.4310076

Polak, M., Starmer, W.T., 2001. THE QUANTITATIVE GENETICS OF FLUCTUATING ASYMMETRY. evol 55, 498–511. https://doi.org/10.1554/0014-3820(2001)055[0498:TQGOFA]2.0.CO;2

Posnien, N., Hopfen, C., Hilbrant, M., Ramos-Womack, M., Murat, S., Schönauer, A., Herbert, S.L., Nunes, M.D.S., Arif, S., Breuker, C.J., Schlötterer, C., Mitteroecker, P., McGregor, A.P., 2012. Evolution of eye morphology and Rhodopsin expression in the Drosophila melanogaster species subgroup. PLoS ONE 7, 1–11. https://doi.org/10.1371/journal.pone.0037346

Ramaekers, A., Claeys, A., Kapun, M., Mouchel-Vielh, E., Potier, D., Weinberger, S., Grillenzoni, N., Dardalhon-Cuménal, D., Yan, J., Wolf, R., Flatt, T., Buchner, E., Hassan, B.A., 2019. Altering the Temporal Regulation of One Transcription Factor Drives Evolutionary Trade-Offs between Head Sensory Organs. Developmental Cell 780–792. https://doi.org/10.1016/j.devcel.2019.07.027

Ramirez-Esquivel, F., Ribi, W.A., Narendra, A., 2017. Techniques for Investigating the Anatomy of the Ant Visual System. J Vis Exp 56339. https://doi.org/10.3791/56339

Ready, D.F., Hanson, T.E., Benzer, S., 1976. Development of the Drosophila retina, a neurocrystalline lattice. Developmental Biology 53, 217–240. https://doi.org/10.1016/0012-1606(76)90225-6

Reis, M., Wiegleb, G., Claude, J., Lata, R., Horchler, B., Ha, N.-T., Reimer, C., Vieira, C.P., Vieira, J., Posnien, N., 2020. Multiple loci linked to inversions are associated with eye

size variation in species of the Drosophila virilis phylad. Scientific Reports 10, 12832. https://doi.org/10.1038/s41598-020-69719-z

Schindelin, J., Arganda-Carreras, I., Frise, E., Kaynig, V., Longair, M., Pietzsch, T., Preibisch, S., Rueden, C., Saalfeld, S., Schmid, B., Tinevez, J.-Y., White, D.J., Hartenstein, V., Eliceiri, K., Tomancak, P., Cardona, A., 2012. Fiji: an open-source platform for biological-image analysis. Nature Methods 9, 676–682. https://doi.org/10.1038/nmeth.2019

Warrant, E.J., 2008. Seeing in the dark: Vision and visual behaviour in nocturnal bees and wasps. Journal of Experimental Biology 211, 1737–1746. https://doi.org/10.1242/jeb.015396

Warrant, E.J., Nilsson, D.E., 1998. Absorption of white light in photoreceptors. Vision Res 38, 195–207. https://doi.org/10.1016/s0042-6989(97)00151-x

Warren, J., Kumar, J.P., 2023. Patterning of the Drosophila retina by the morphogenetic furrow. Frontiers in Cell and Developmental Biology 11.

Wolff, T., Ready, D.F., 1993. Pattern formation in the Drosophila retina, in: The Development of Drosophila Melanogaster. Cold Spring Harbor Laboratory Press, pp. 1277–1325.